Principles of Computer Numerical Controlled Machining Applied to Small Research Animal Microsurgical Procedures

A THESIS
SUBMITTED TO THE FACULTY OF THE GRADUATE SCHOOL OF THE UNIVERSITY OF MINNESOTA
BY

Mathew Lavere Rynes

IN PARTIAL FULFILLMENT OF THE REQUIREMENTS
FOR THE DEGREE OF MASTER OF SCIENCE

Prof. Suhasa B. Kodandaramaiah

December 2017

Acknowledgements

I would like to acknowledge Leila Ghanbari, whose idea motivated this research and enabled us to explore the initial idea. She designed, implemented and collected data for all of the prototype work presented in Chapter 2 of this thesis.

I would also like to acknowledge Gregory Johnson, who completed most of the initial engineering in building the Craniobot. Greg's knowledge and creativity made this project possible.

I would like to thank Jay Jia Hu and Daniel Sousa Schulman as well. Jay helped engineer the surface profiler and worked very closely with me in designing the experiments characterizing the contact sensor and taking data. Daniel also was of tremendous help in diligently measuring many samples after experiments had been conducted, statistical analysis of the results, and development of the software.

I am very grateful to Professor Suhasa Kodandaramaiah and my colleagues in his lab group, whom this would not have been possible without. Suhasa constantly pushed me to improve myself, and my lab mates in Prof. Kodandaramaiah's lab group were always encouraging and helpful.

I am also grateful to Prof. Alptekin Aksan, who introduced me to Suhasa. Not only have I learned a lot from Prof. Aksan, but he has also helped me improve myself both as a scientist and as a hard worker.

I would like to acknowledge our research partners at the Minnesota Nano Center and the Minnesota Dental Research Center for Biomaterials and Biomechanics for assisting us in making measurements of our samples.

Finally, I would like to thank all of my friends, and most of all my family. Without support from my brothers, my parents and my close friends, my journey to discover more about the world would have been much more difficult.

Table of Contents

List of Tables

List of Figures

Chapter 1 Introduction

The palette of tools available for systems neuroscientists to measure and manipulate the brain during behavioral experiments has exploded in the last decade. Traditionally, many neuroscience experiments were accomplished by sensing electrical signals from neural activity, while neuromodulation was achieved using chemicals and electrical manipulation. Recording experiments were typically done with simple tungsten electrodes and wires (Hubel, 1957), and evolved to silicon-based 3-dimensional (3D) electrodes for higher spatial resolution over large volumes (Jun et al., 2017; Scholvin et al., 2016). Recent advances in fabrication techniques and materials have enabled the development of high density probes and neural meshes, which further increased recording capabilities over larger volumes of the cortex while minimizing inflammatory response (Liu et al., 2015; Viventi et al., 2011; Yazicioglu et al., 2014). These have been implemented on electrode technologies such as injectable neural mesh electrodes for easier introduction into the cortex (Yazicioglu et al., 2014), high-density silicon electrode arrays for increased spatial resolution (Blanche, 2005), and 3D organic electrodes (Khodagholy et al., 2016). However, one limitation of electrical sensing is that it requires relatively invasive procedures compared to other recording modalities with a higher risk of causing chronic damage to brain tissue, and this has prompted exploration of other neural interfacing methods.

The development of optical sensing, modulation and manipulation has enabled neuroscientists to investigate the brain at different scales across multiple regions. In this newly emerging space of optical interfacing with neurons, or optogenetics (Boyden, Zhang, Bamberg, Nagel, & Deisseroth, 2005), newly developed technologies allowed for

a wider range of targeted manipulation of neurons in the brain, ranging from large volumes of tissue to more spatially defined volumes via optical fibers (Pisanello et al., 2017). The development of chronically stable fluorescent activity reporters such as the GCaMP family of calcium dependent fluorescent proteins have also enabled researchers to investigate wide regions of the brain at cellular or near-cellular resolution in behaving animals (Kim et al., 2016; Zong et al., 2017).

A common theme with advances in tools for recording and stimulation in behaving animals are the respective surgical methodologies that have evolved. The advantages presented by each tool results in challenges unique to each corresponding surgical procedure. For instance, large 3D electrode arrays need ways to precisely pattern craniotomies through which the arrays can be inserted. Ultra-wide field calcium imaging requires surgical procedures for large cranial implants, which require a variety of skull excisions that can encompass large sections of the dorsal skull (Kim et al., 2016). Intact skull preparations have become commonly used for optical imaging on mice, which requires the skull to be thinned on the order of tens of micrometers (Drew et al., 2010; Shih, Mateo, Drew, Tsai, & Kleinfeld, 2012; Silasi, Xiao, Vanni, Chen, & Murphy, 2016). The growing viability and use of *in vivo* patch clamping (Margrie et al 2013) and its automation (Kodandaramaiah, Franzesi, Chow, Boyden, & Forest, 2012; Suk et al., 2017) rely on pristine surgical preparation for success (Kodandaramaiah et al., 2016). These procedures require the removal of bone tissue without damage to the underlying brain tissue (Wang, 2016).

Microsurgical procedures in neuroscience laboratories have been developed by adapting tools and tissue removal processes from dentistry. Dental drills fitted with dental burr drill bits are commonly used for removing bone tissue. This is typically a delicate

procedure as the skulls of commonly used inbred mouse strains, such as C57BL/6J mice, are very thin, ranging from roughly 50-500 μm above the dorsal cortex. Devices are fixed to the skull using dental cement (Drew et al., 2010; Holtmaat et al., 2009). However, with increasing complexity, these microsurgical procedures have become art forms. The techniques are hard to master have a very high entry barrier, as it takes many months to become skilled at performing these operations, which end up often confined to a select few lab groups. Manual microsurgical procedures are prone to high variability from experimenter and experimenter. This complexity precludes neuroscientists from exploring more challenging surgical procedures, thus limiting the pace of advancement of neuroscience research. Automating some of the tissue removal processes would potentially enable more precise procedures to be performed as well as democratize advanced surgical processes.

Automating surgical procedures has been explored to an extent by adapting commercially available stereotaxic surgery tools to motorized stages. (Pak et al., 2015). While previous automation efforts for microsurgery have focused on incorporating hardware and software into existing stereotaxic apparatus, an alternate approach that integrates surgical capabilities into computer numerically controlled **(**CNC) precision machining apparatus would enable unique advantages. Precision CNC machining tools are available for a wide range of fabrication procedures, from hobby machining to mass production. These machining tools have an ecosystem of optimized algorithms and programming languages, all of which are highly developed, accessible and readily available in a wide range of configurations to perform a variety of machining tasks. In principle, these tools can be adapted for automating microsurgery, enabling neuroscientists to perform delicate procedures precisely and potentially derive more complex procedures. Furthermore, since these tools have a wide user base, they are

relatively inexpensive. The prices of precision machining tools have rapidly decreased in recent years. For instance, the cost of desktop 3D printing tools have fallen by half over the past decade (Agiimaa Kruchkin, 2016) leading to widespread adoption. Thus, this strategy of using readily available, inexpensive, desktop machining tools has the potential to realize low cost, versatile automated platforms for neuroscientists, and clinical applications.

Here, we introduce the 'Craniobot', a microsurgery platform that combines automated skull surface profiling with a CNC milling machine, typically used by woodworking hobbyists, to perform a variety of microsurgical procedures in mice. We demonstrate the Craniobot's ability to precisely perform microsurgical procedures such as skull thinning, small to large craniotomies of digitally defined shapes on the dorsal skull, as well as drilling pilot holes for anchoring cranial implants. The Craniobot can accomplish these tasks while being assembled with off-the-shelf components for under $1000. By adapting CNC machines to perform a wide range of procedures at such a low cost, the Craniobot opens the possibility of democratizing and streamlining complex *in vivo* neuroscience procedures. Considering we are using open source and customizable machining practices, this approach can be expanded in the future to larger animal models, or for more complex procedures and a more comprehensive part of the pipeline of *in vivo* neuroscience.

Chapter 2 Surface profile guided skull machining: preliminary investigations

2.1 Experimental design

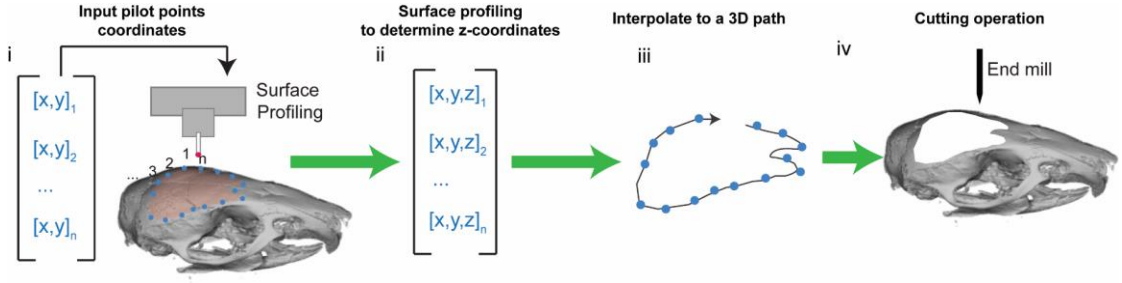

Figure 2.1: Principle of operation of CNC milling. Given a desired craniotomy profile, a surface profiler can be used to gather z-coordinates from the surface of the skull at a set of pilot points lying along the boundary of the craniotomy. This information can be used to interpolate a 3D cutting path to guide a CNC end mill.

We hypothesized that if an apparatus could be built to precisely determine the coordinates of select pilot points on the surface of the skull, it would be possible to interpolate a 3D trajectory for guiding a computer controlled cutting tool (**Fig. 2.1**). As the average thickness of the skull is relatively conserved within each mouse strain (e.g., C57BL/6J) at a certain age and sex, a topographic map of the top surface of the skull is sufficient to perform skull excisions by iteratively milling down to increasing depths. If the depth of milling is less than the thickness of the skull at any point along the desired cutting path, the skull can be thinned down to a point where it can be excised without damaging the underlying tissue. To test this, we build a simple motorized manipulator guided end mill and incorporated it into a standard rodent stereotax.

2.2 Methods: Robot construction and operation

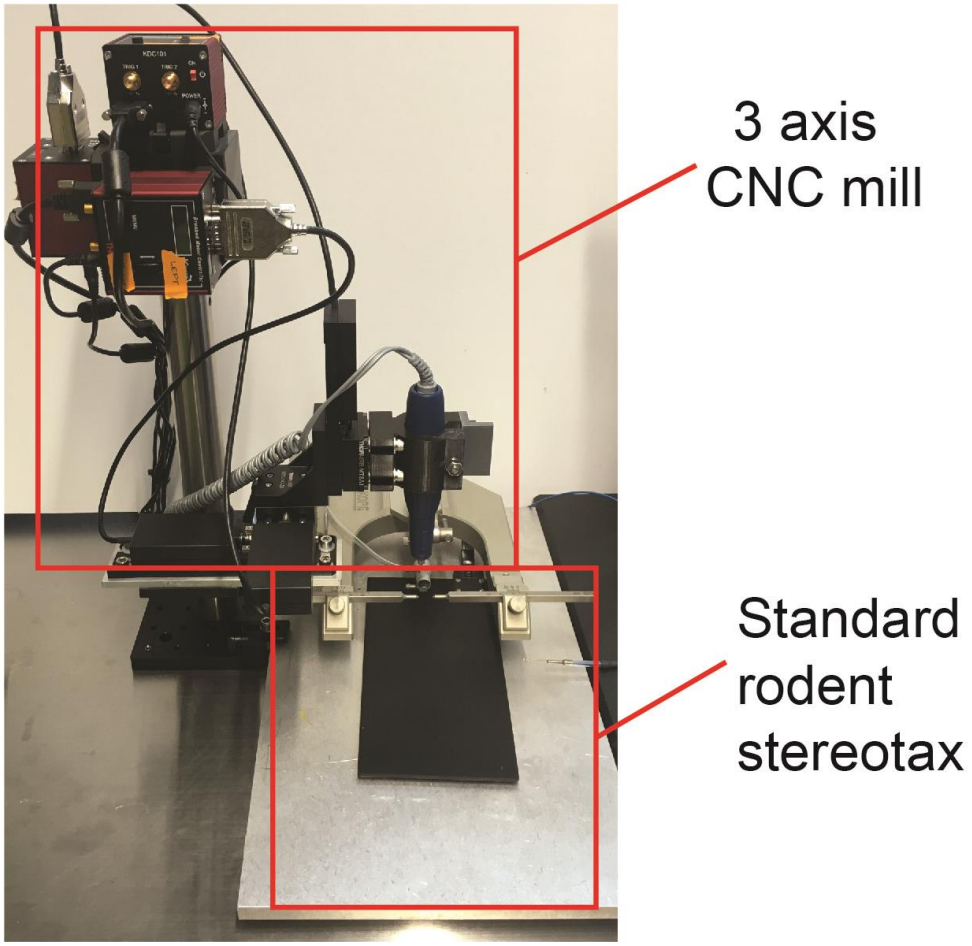

Figure 2.2: Prototype craniotomy robot in a standard rodent stereotax.

This prototype craniotomy robot was realized by incorporating 3-axis motorized manipulator (MTS25-Z8, Thorlabs) into a standard rodent stereotax (David Kopf Instruments Inc.) (**Fig. 2.2**). A custom mounting clamp was used to attach a handheld mill (Rampower, Ram Products Inc.) to a 3-axis stage. A 200 µm diameter end mill (13908, Harvey Tool Inc.) was fitted to the end of the CNC-guided handheld mill as a cutting tool. The CNC was controlled via a custom software suite written in LabVIEW (National

Instruments Inc.). The skull surface profiling was performed in this step by the experimenter guiding the end mill to the surface of the skull after the program guides it to each x-y pilot point while observing through a stereomicroscope and registering the z coordinate. After all points are registered, the program generates a 3D cutting path by interpolating the coordinates and increasing the depth of the z-coordinate by 80 μm. The end mill would then machine the skull at this depth along the cutting path. After this, the experimenter would verify if the milled bone is fragile enough to be fractured and removed. If it was not ready to be excised, the program would give the experimenter the option of beginning another milling iteration. The software contained code that lowered the tip by 10 μm for each successive iteration, and this process could be repeated until the bone fragment was ready to excise.

2.3 Results

The CNC guided end mill could perform skull machining operations with qualitatively observable accuracy. As an illustration, we could perform an 80 μm deep milling operation tracing the university of Minnesota logo **(Fig. 2.3b)**.

We then used this prototype craniotomy robot to perform skull excisions across the whole dorsal cortex. 30 to 38 x-y pilot points spaced approximately 0.5 mm apart were used to define a craniotomy covering bilateral motor, somatosensory, granulate and visual cortices. Further, the trajectory could be programmed to avoid major sinuses present in the bone along the midline suture 2-3 mm anterior to bregma. Once the z-coordinates

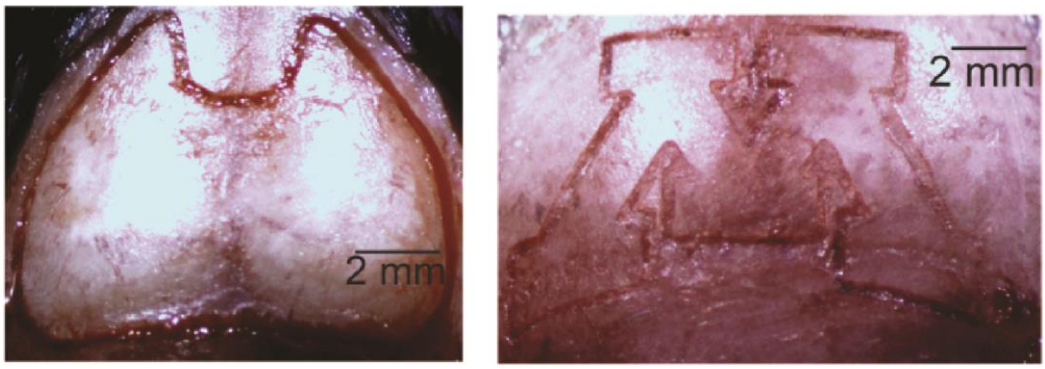

Figure 2.3: Representative illustrations of milling operations performed by the prototype craniotomy robot. (a) A craniotomy performed across the whole dorsal cortex while avoiding major sinuses anterior to bregma along the midline suture. (b) Engraving the University of Minnesota logo into the dorsal surface of the skull.

were mapped, we performed an iterative milling procedure. In the first pass, milling was performed down to a depth of 80 μm from the surface. This was followed by manual inspection to check if the bone was fragile enough to be fractured and excised. If not, the subsequent passes were attempted at increments of 10 μm until the skull was loose enough to be pried open. An illustration of such a procedure after the first pass is shown in **Figure 2.3**. We performed this CNC milling procedure in 13 wild type C57BL/6J mice ages 7 to 13 weeks, and 6 transgenic Thy1-GCaMP6f mice ages 10 to 14 weeks. Both male and female GCaMP6f mice were used. Following the craniotomy, the excised bone tissue was cleaned in saline, and we measured the thickness of the skull at five points shown in **Figure 2.4** with a caliper. In all the experiments, the iterative milling procedure was stopped at a depth consistently less than the minimum thickness of the skull. On average, the final drilling depth was 56.1 ± 30.4 μm less than the minimum thickness in wild type mice and 146.6 ± 25.2 μm in Thy1-GCaMP6f mice. This confirms that we could

avoid contacting the underlying brain tissue in all experiments using the prototype craniotomy robot.

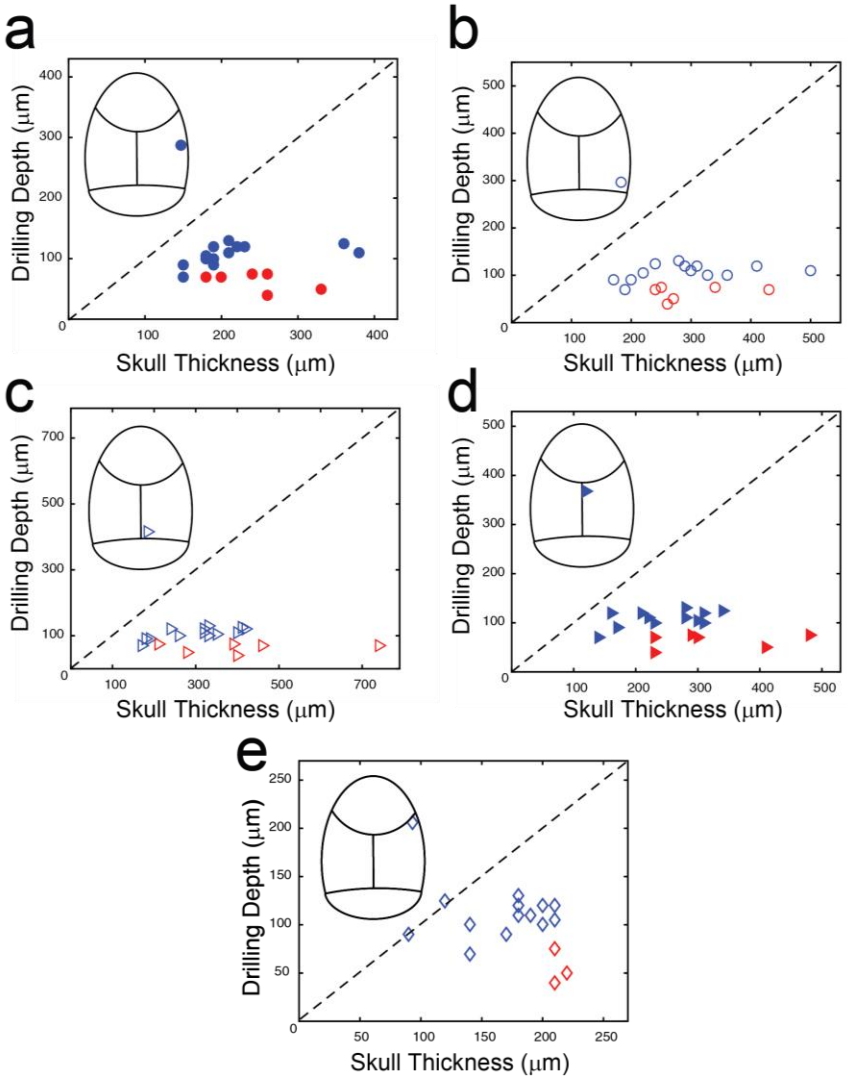

Figure 2.4: Final drilling depth vs skull thickness. After craniotomies using the prototype craniotomy robot, the excised skull fragments were collected and measured at various regions: **(a)** roughly 4.5 mm lateral from bregma, **(b)** roughly 4 mm lateral from lambda, **(c)** roughly at lambda, **(d)** roughly at bregma and **(e)** roughly 2 mm lateral and 2.5 mm anterior to bregma. Blue data points indicate measurements in male wild type C57BL/6J mice, and red data points indicate measurements in transgenic Thy1-GCaMP6f mice – both male and female. 3 data points are missing in (e) due to damage to the skull during the excision process.

The results of the experiments indicated that surface profiling guided CNC machining was a viable method of performing automated craniotomies. This setup is currently being used in our laboratory to create large craniotomies. However, there are a couple drawbacks. First, the time taken for surface profiling varied from person to person depending on experience. Second, the contact made by the tip of the milling tool was visualized through a stereomicroscope, which was subjective. Thus, we wanted to explore a more streamlined method to accomplish this. This is presented in the following chapters.

Chapter 3 Craniobot design and operation

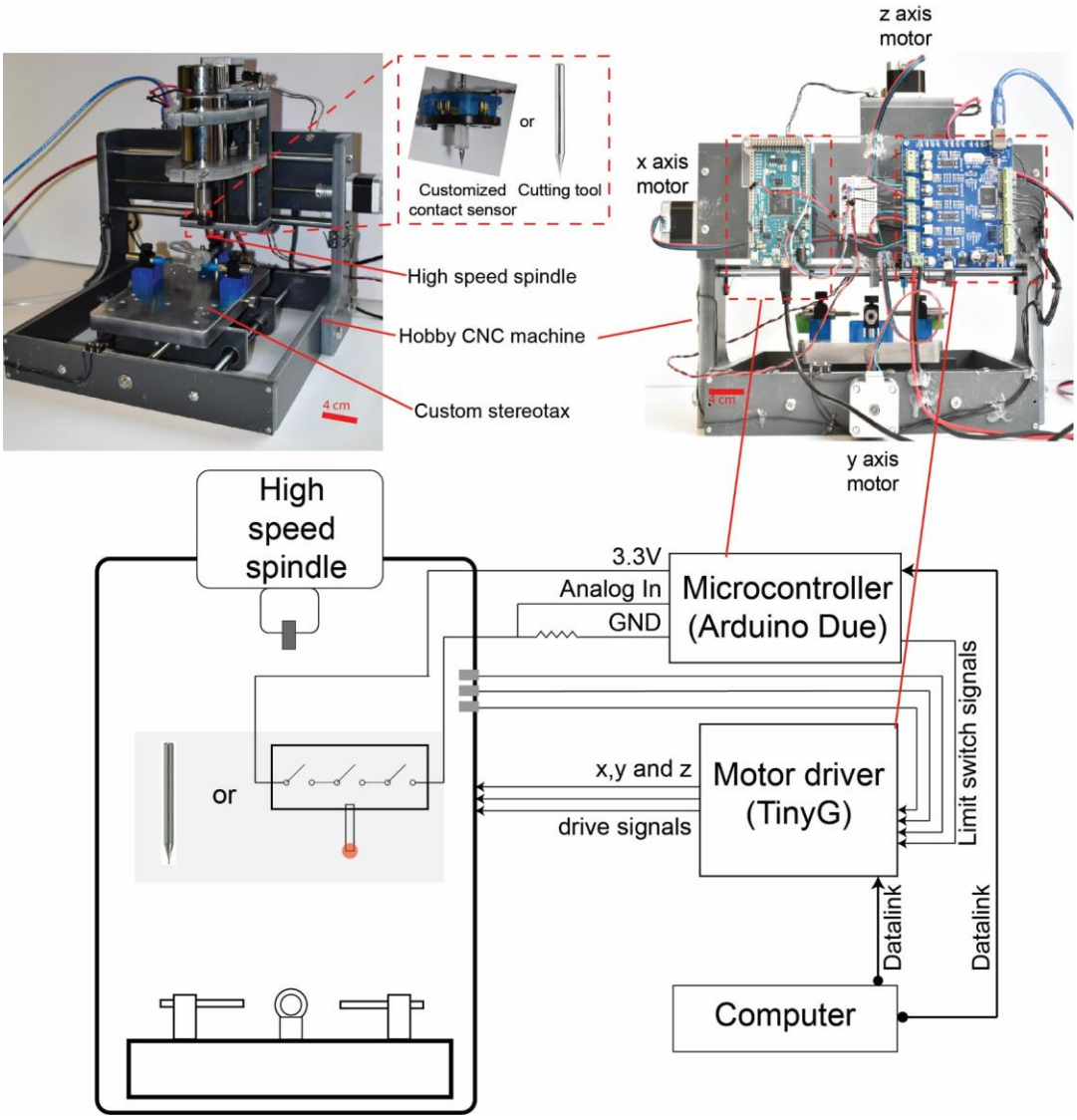

Figure 3.1: Craniobot hardware. The Craniobot is built by adapting a hobby CNC milling machine with a custom-built stereotax, a customized contact sensor, and open source motor drivers, and a microcontroller that interfaces contact sensor with a computer.

To address limitations of the prototype craniotomy robot, we set out to automate the surface profiling step. Given the widespread use and capabilities of CNC machining apparatus, we decided that adapting a CNC mill to perform microsurgical procedures

would be the simplest and most robust approach. To accomplish this, we needed tools that could be readily adapted for microsurgical procedures: a machining mill base that fits a mouse, a device capable of detecting surfaces, and a combination of software and hardware to control and interface with the microsurgery platform. The Craniobot design incorporates a 3-axis hobby machining mill (Lukcase LC8110), an open source USB motor controller (TinyG v8), a custom contact sensor modified from an industrial digitizing surface probe (Tormach SPU-40) monitored via analog input form a microcontroller (Arduino Due), and a Python 3.6 software suite (**Fig. 3.1**). A custom-built 3D printed and machined stereotax base was modified into the bed of the mill. These tools fulfilled the stated necessary requirements to automate the surface profiling and milling. In the following section, we describe the details of each core component.

3.1 CNC mill base and stepper motors

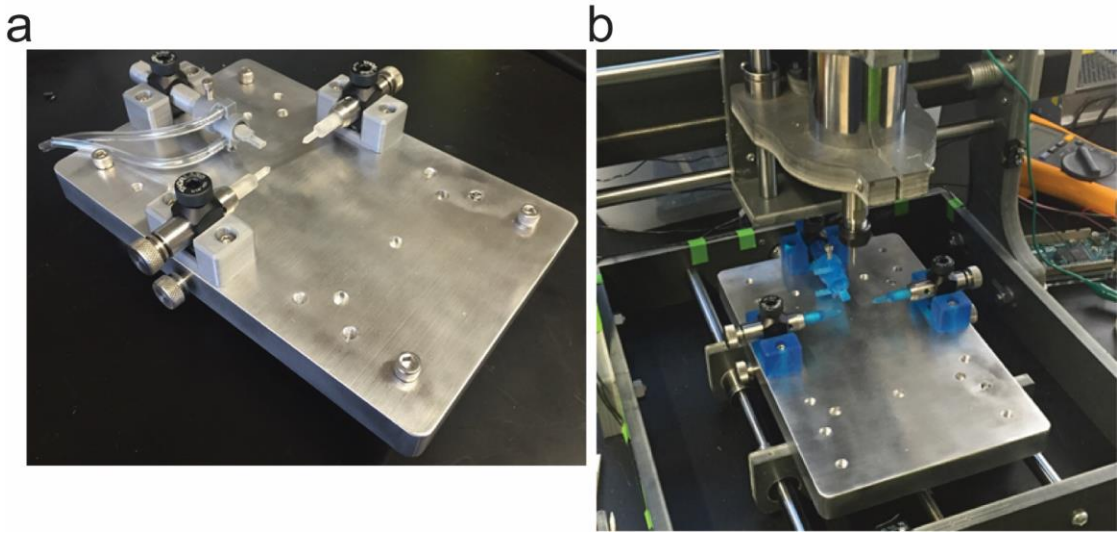

Figure 3.2: Custom stereotax. (a) Shows the custom stereotax, and (b) depicts it integrated into the hobby CNC milling machine in the Craniobot.

The 3-axis hobby machining mill used as the base machine for the Craniobot is widely sold by a variety of manufacturers online, but is generically called a 2020B CNC

mill, which refers to the size of the x-y bed of the machine (20cm x 20cm). The frame of the mill was modified to include a home-built custom stereotax in place of the bed of the stock machine using a combination of 3D printed ear and mouth bar components, machined components, and off the shelf hardware. The mill framework is made from machined plastic, and the moving axes are guided along stainless-steel shafts and linear bearings pressed into the framework components. 3D positioning is accomplished by three NEMA 17 stepper motors and M8 stainless steel leadscrew assemblies. The leadscrews couple to each moving axis by anti-backlash nuts, which improves the overall precision of the machine.

The custom stereotax was constructed by first machining a base out of a 0.75-inch thick aluminum block using abrasive water jet machining. Holes were water jet cut, drilled,

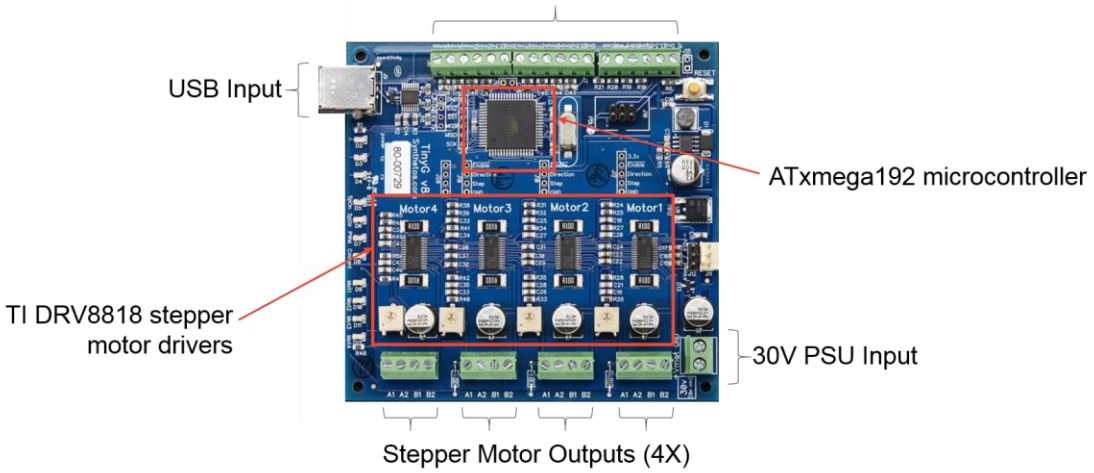

Figure 3.3: Tiny G printed circuit board and components.

and then tapped into the aluminum base to fit the stereotax pieces and mount it on the mill base. The base was finished with a wire wheel brush to smoothen out the surface. The stereotax parts were made via a combination of 3D printed parts, off-the-shelf

components, and machined parts for added stability. The completed custom stereotax for the CNC is depicted in **Figure 3.2**.

3.2 Electronics

We replaced the factory electronics included in the hobby mill with an open source stepper motor controller that is widely available and has an active online development community (TinyG, Syntheos). It combines a microcontroller (Atmel ATxmega192) and four stepper motor drivers (TI DRV8811) onto a single printed circuit board and USB interface. A diagram of the components on the TinyG is shown in **Figure 3.3**.

Communication to and from the machine is accomplished over USB, and formatted using standardized CNC G-code language packaged inside JavaScript Object Notation (JSON) text strings. The entire robot is operated through a software suite we created in Python 3.6, which generates, sends and receives commands and communications with the Craniobot. First, the software generates the x-y coordinates of a craniotomy based upon user inputs (i.e. a 3-mm diameter circular craniotomy offset 1.5mm from bregma, or a whole-dorsal skull craniotomy with a custom shape) and formats these in G-Code-based JSON strings. The Craniobot then uses the customized contact sensor to scan for the z coordinate at each point.

3.3 Custom contact sensor

We first needed a method to automatically profile the skull surface. Typically, in precision machining, this is accomplished using digitizing surface profilers. However,

commercially available surface profilers are intended for use as industrial metrology devices, and, thus, have a large actuation force. For example, the Tormach SPU-40 had an actuation force specified by the manufacturer as 570g – far too high for use as a mouse

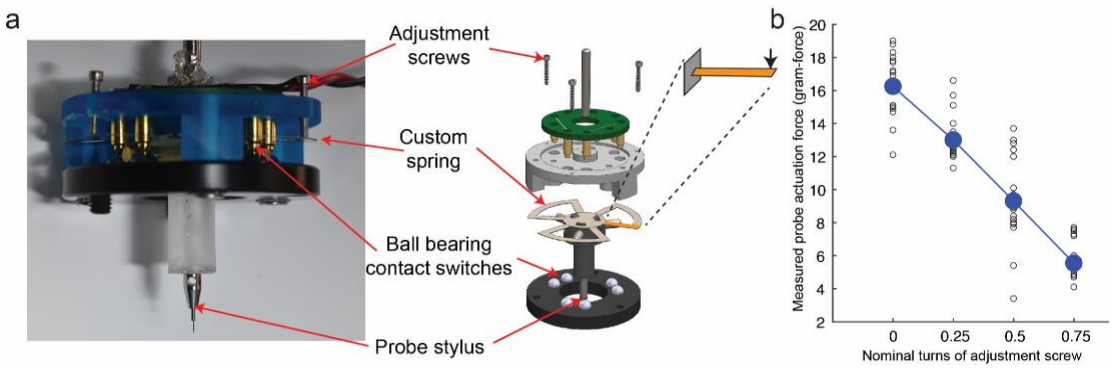

Figure 3.4: Custom contact sensor. (a) Depicts the contact sensor's components alongside a CAD illustration of the components. A 300 μm ruby-sphere stylus is shown attached to the end of the contact sensor. We designed the custom spring by modeling each radial arm as a cantilever beam. (b) The actuation force as a function of the nominal turns of the adjustment screws shows a linear relationship. We used the custom contact sensor at an actuation force ranging from 5-10g force.

skull surface profiler. We, therefore modified the digitizing surface profiler by removing the stock compression spring and replacing it with a custom waterjet-cut stainless steel spring. We further 3D printed a new housing that allowed us to adjust actuation force with #0-80 screws. The resulting design is illustrated in **Figure 3.4**.

The contact sensor electronics consists of three normally closed switches connected in series. Each switch consists of two spherical stainless-steel contacts electrically bridged by a brass cylindrical arm. The three arms are pressed into the probe tip assembly, and this assembly nominally rests on the three sets of spherical ball contacts creating a normally closed switch circuit. When the probe tip contacts the mouse skull, one of the arms lifts off the spherical contacts and open the circuit. The internal customized spring presses the tip assembly onto the contacts and improves contact resistance.

To calibrate the contact sensor, we estimated the spring force and the resulting actuation force, and then conducted a set of experiments testing the actuation force per turn of the adjustment screws. We estimated the spring force by assuming that the deflection in the radial leaves of the cantilever spring contributed the most to the spring force, and that any torsion in the radial arms or bending of the arc component contributed with a negligible amount of spring force. We expected these assumptions to lead to a stiffer estimated spring force than what we would measure. The spring deflection in each cantilever arm is given by:

$$y = \frac{PL^3}{3EI}$$

Where P is the force onto the end of the cantilever arm, L is the length of the cantilever, E is the Young's modulus of the material, and I is the moment of inertia of the cross section about its normal axis. Given that there are 6 radial arms, if F is the total tip actuation force, we get:

$$F = 6P$$

Therefore, we have the deflection as a function of the actuation force given by:

$$y = \frac{FL^3}{18EI}$$

The spring force in our system could be adjusted by threading in #0-80 screws, which have a pitch of 3150 turns/m. Based on the dimensions and the spring steel used, we estimated that the actuation force would increase by ~20g force per turn of the adjustment screws. We tested this by commanding the Craniobot to probe a single point on a weighing scale for multiple replicates while adjusting the screws by a quarter turn for

each condition (**Fig. 3.4b**). From these experiments, we found that the actual actuation force varied by ~14.5g force per turn.

This design resulted in an order of magnitude reduction in actuation force. We tested the contact sensor on a mouse skull securely fixed on a stereotax, and found that a total force of 5-10g was appropriate for skull surface profiling. Using such a light actuation force causes the contact resistance inside the probe to be high enough (1-5 kΩ) that the probe can no longer be used in a simple passive switch circuit. We instead placed the probe in series with a 1 kΩ resistor, creating a voltage divider that was monitored using an analog input on a microcontroller. An analog voltage threshold on the microcontroller determined if the probe had been actuated and sends this information to the motor controller.

Using the contact sensor in this manner, the skull profiling operation can be fully automated by sending the motor controller an x-y coordinate, requesting the machine to probe downward at that position until the probe switch state changes, and reading back the z coordinate at which the state change happens. By repeating this process over a complete set of x-y coordinates, the skull surface contour could quickly be mapped in three dimensions, and the information could be used for microsurgery.

3.4 Operation

The Craniobot functions via automating two major processes: profiling the skull surface and using that information to perform CNC milling.

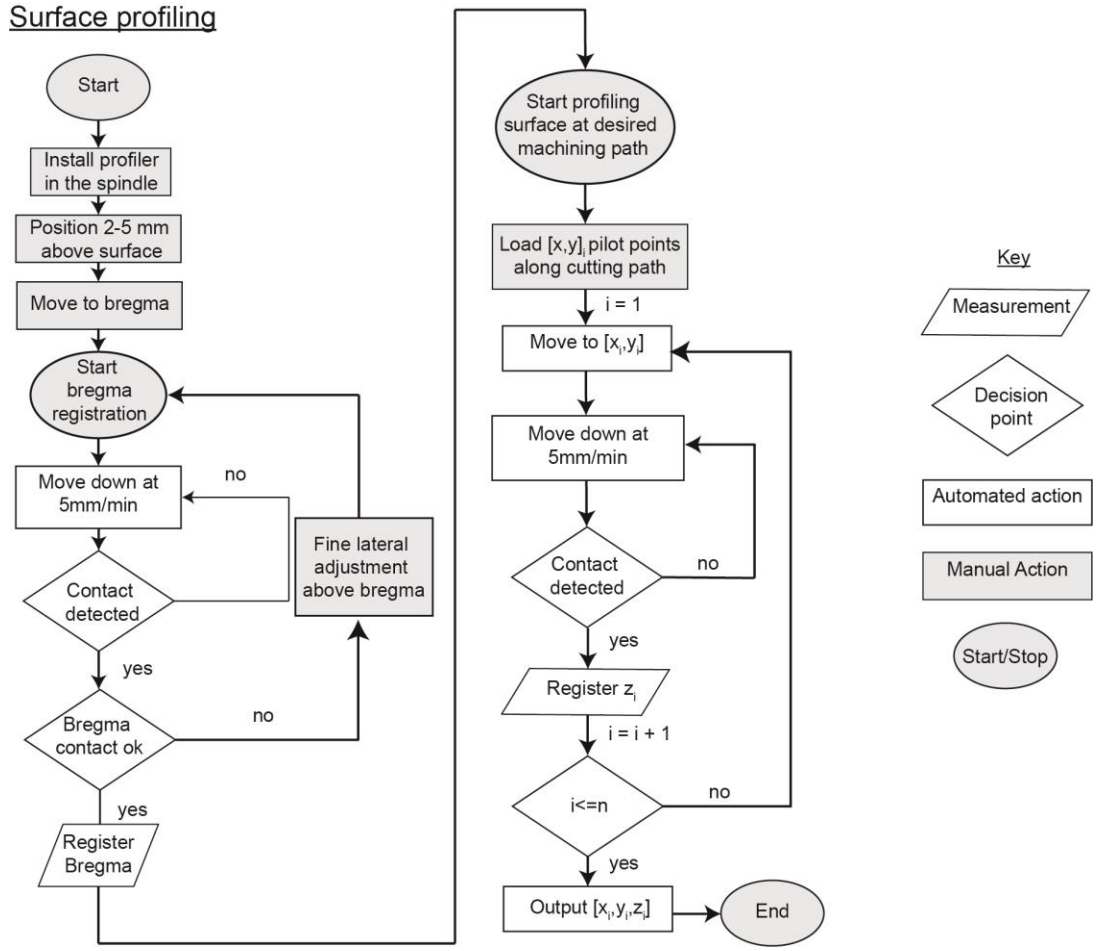

Figure 3.5: Flowchart of the surface profiling process. The major steps in the surface profiling process are illustrated here. After the profiler is installed in the spindle, the experimenter positions it over bregma. Upon running a script, the Craniobot moves the contact sensor down until it meets the skull surface at bregma. If needed, fine lateral adjustments can be made to insure proper localization to bregma. Then the bregma coordinates are registered. The x-y coordinates of the pilot points are inputted by the experimenter, and the Craniobot uses them to guide the contact sensor to measure the z coordinate at each point. The information is then outputted to a container variable in the Python software suite to generate a milling path.

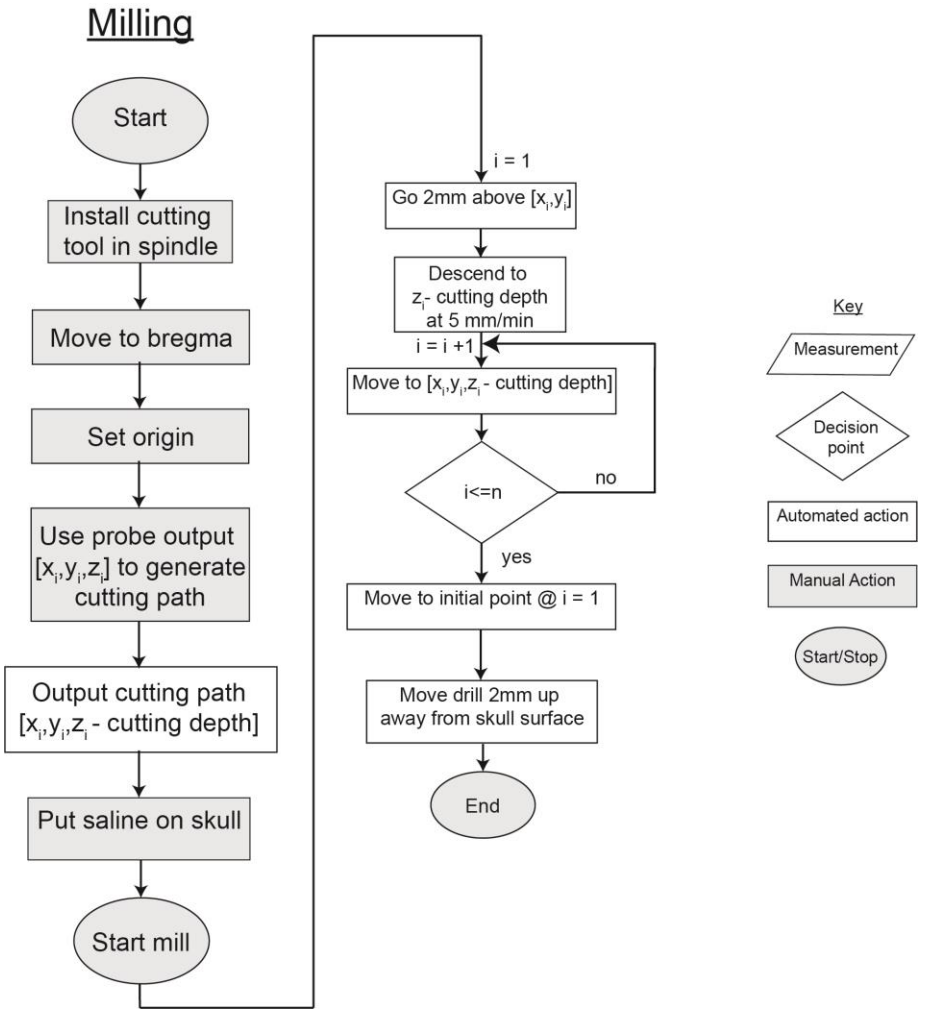

Figure 3.6: Flowchart of the automated milling process. The major steps of the automated CNC milling are illustrated here. The experimenter begins the milling by placing the desired cutting tool into the spindle. The cutting tool must be then guided carefully to the surface of the skull at bregma. When this is complete, the experimenter can then use the data output from the surface profiling to generate a 3D linearly-interpolated milling path, which the Craniobot then uses to guide the end mill to perform the cutting procedure.

The operation of the Craniobot's surface profiling is illustrated in flowchart form in **Figure 3.5**. To begin surface profiling, the experimenter installs the contact sensor into the spindle and positions it 2-5 mm above the surface by sending jog commands into the software suite. Lateral adjustments are made so that the sensor is positioned directly above bregma. After the contact sensor is positioned directly above bregma, a script is

initiated to register bregma. The Craniobot moves the contact sensor down at 5 mm/min while constantly sensing the switch signal attached to the sensor. Once contact is detected, the bregma coordinates are registered as the origin of a Cartesian coordinate system. After bregma is registered as the origin, the Craniobot uses a desired path of points loaded into the software suite by the experimenter to systematically profile the z coordinate at each x-y point in the desired cutting path. After the Craniobot finishes the automated surface profiling, it outputs a 3D set of points from the collected z coordinate at each pilot point. At this point, the user can check the 3D points to ensure that there aren't any false positives that interfere with the completion of the microsurgical procedure.

After the Craniobot finishes surface profiling, the experimenter can begin the Craniobot's automated milling process. A flowchart illustrating the milling process is shown

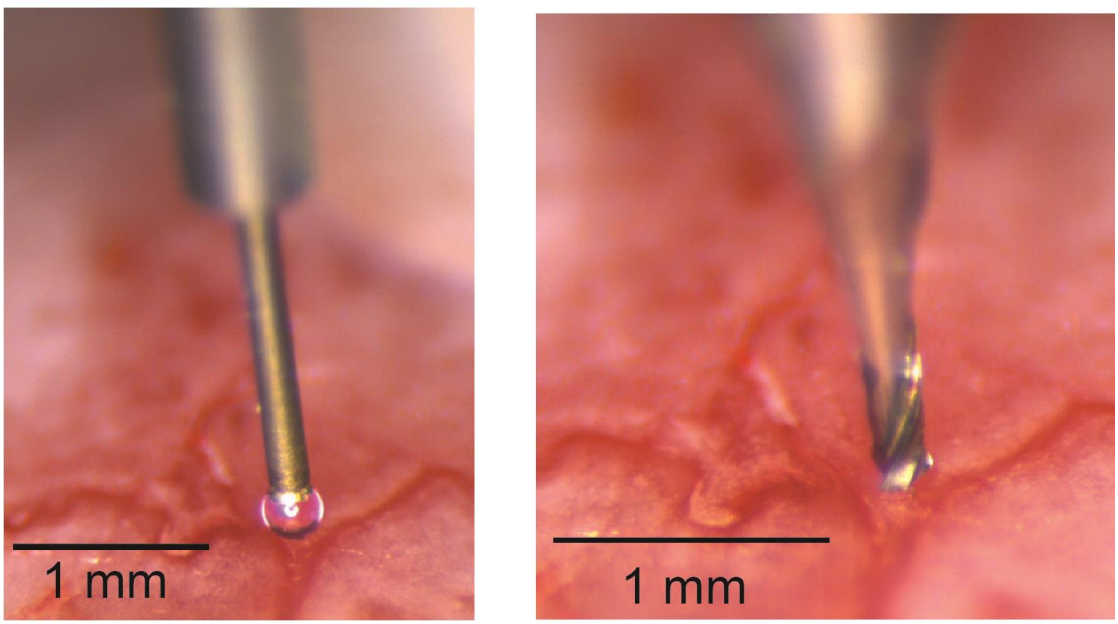

Figure 3.7: Re-registration of bregma after surface profiling. (a) A photograph of the 300 μm ruby-sphere stylus automatically guided to bregma via contact sensing, and (b) shows a 200 μm square-end mill visually guided to the same location prior to milling.

in **Figure 3.6**. The first step is to change the tool; since the tool at the end mill is changed from the contact sensor to a cutting tool, bregma must be re-registered. The experimenter must carefully guide the cutting tool to bregma, matching the location of the initial probing point at bregma. This is performed while observing the end mill through a stereo microscope and sending jog commands through the software. Photographs can be used to assist the experimenter in placing the cutting tool at the same location as the contact probe at bregma as illustrated in **Figure 3.7**. After the tool is placed at bregma, the experimenter registers bregma as the origin of a new coordinate system for milling. Next, to begin milling, the experimenter uses an automatically generated linearly-interpolated cutting path from the surface profiling output data to begin the automated milling process. Saline is used as a coolant and to remove tissue debris during the milling process. The Craniobot then guides the tool through the automatically generated milling path until it reaches the final point. At the end of the milling path, if a craniotomy is being milled, it will return to the original point to close a craniotomy, and then raise the tool 2 mm above the surface of the skull and stops. At this point, the experimenter can freely move the tool away from the skull for inspection, or begin another milling run at higher depth, in this way performing an iterative milling process.

Chapter 4 Performance of automated surface profiling

4.1 Methods

4.1.1 Surgical procedure

All animal experiments were conducted in accordance with approved UMN IACUC protocol. Characterization and demonstration experiments were conducted in acute anesthetized conditions. Mice (C57BL/6J, 8-14 weeks old) were administered buprenorphine (Par Pharmaceutical, Chestnut Ridge, NY) at 1 mg/kg body weight, and meloxicam (Dechra Veterinary Products, Overland Park, KS) 1-2 mg/kg body weight at the time of the experiment. Mice were anesthetized with 1-5% isoflurane (Piramal Critical Care Inc., Bethlehem, PA), the fur was removed from the scalp, and the mouse was placed on the custom stereotaxic apparatus. Standard aseptic techniques were used to sterilize the scalp area before the incision. The skin and fascia were then carefully removed around the targeted cutting path. All procedures were performed with aseptic techniques. For characterization experiments, mice were euthanized and perfused immediately upon the completion of the procedure. This was followed by a variety of experiments that were used to characterize the performance of the contact sensor, characterize the ability of the CNC mill to use the surface profiling information in microsurgical procedures, and demonstration experiments.

To profile the skull surface, the needle tip (II M2 030 03 015, ITP Styli LLC, St Louis, MO) or ruby sphere (TH M2 003 03 010, ITP Styli LLC, St Louis, MO) stylus were sterilized with 70% ethanol, washed with saline, and attached to the end of the custom contact sensor, and the contact sensor was fitted to the end of the spindle. This was then used to measure the points in the milling path, which were spaced out with a maximum distance of 0.5 mm. The tool was then switched to a cutting tool and the cutting operation was performed. We used a 200 μm diameter square end mill, and a 300 μm ball end mill (24512, Harvey Tool Inc.). The milling procedure was completed in iterations increasing the milling depth until the milled skull flap could be fractured and excised.

4.1.2 Perfusion

Following the microsurgical procedures, mice were either euthanized or transcardially perfused to preserve the tissues for further future analysis. Perfusions were performed by first ensuring the animal was deeply anesthetized with 5% isoflurane at 0.6 L/min pure Oxygen. Phosphate-buffered saline (PBS) (CAT# P5493-1L, Sigma Aldrich) was used to flush the circulatory system at a volume of 1 mL/g body weight, and then 4% paraformaldehyde (PFA, CAT# P6148-500G, Sigma Aldrich) was used to fix the tissues. Immediately after the procedure, the skull of the animal was collected and kept in a solution of 4% PFA for preservation.

4.1.3 Chronic implantation

For microsurgical procedures involving chronic implantations, slow-releasing buprenorphine (Buprenorphine SR LAB, Zoopharm, Windsor, CO) was administered along with meloxicam two hours before the experiment. The microsurgery was conducted as described in **Section 4.1.1**. In procedures involving the implantation of chronic cranial

windows, 3.3 mm diameter circular craniotomies were performed using the Craniobot. 4 mm diameter glass coverslips (Deckgläser, Marienfeld-Superior Inc.) were placed over the craniotomy and glued using cyanoacrylate glue (Vetbond, 3M, Saint Paul, MN). Dental cement (S380, C&B Metabond, Parkell Inc.) was then used to secure the coverslip to the skull surface. After the implantation was finished, animals were recovered on a heating pad and monitored until they could move autonomously. Meloxicam was administered to mice for 3 days after the experiment along with general monitoring for signs of pain. We performed chronic implantations of glass coverslips in 2 mice using this procedure. We also performed 2 chronic implantations of 3D transparent optical windows developed in our lab to demonstrate the ability of the Craniobot to perform complex microsurgical procedures

4.1.4 Micro-CT scanning

We used micro computed tomography (micro-CT) to analyze and reconstruct the 3D skull after the characterization microsurgical procedures. Perfused mouse skulls were cast in acrylic (Dentsply Orthodontic Resin and Caulk, York, PA, USA) on a Teflon pedestal, and images were collected using a Micro-CT machine (XT H 225, Nikon Metrology Inc., Brighton, MI, USA). The x-rays were generated with parameters of 105 kV 85 µA. We scanned the skulls using 720 projections at a half degree pitch while recording 4 frames per projection. Samples were then returned to a solution of 4% paraformaldehyde after scanning.

After finishing x-ray scanning, the micro-CT software reconstructed the x-ray images into a volume graphics file. VG Studio MAX 3.0 was used to denoise unwanted signal caused with a bandpass filter and visualize the 3D structure of the scanned skulls.

The 3D structure of the scanned skulls was then transformed into a cloud of 3D coordinates and then exported as an STL file for further analysis.

4.2 Characterization of contact sensor

We performed contact sensor characterization experiments on skulls of 6 C57BL/6J mice ages 8 -14 weeks. 3 males and 3 females were used. We defined a point

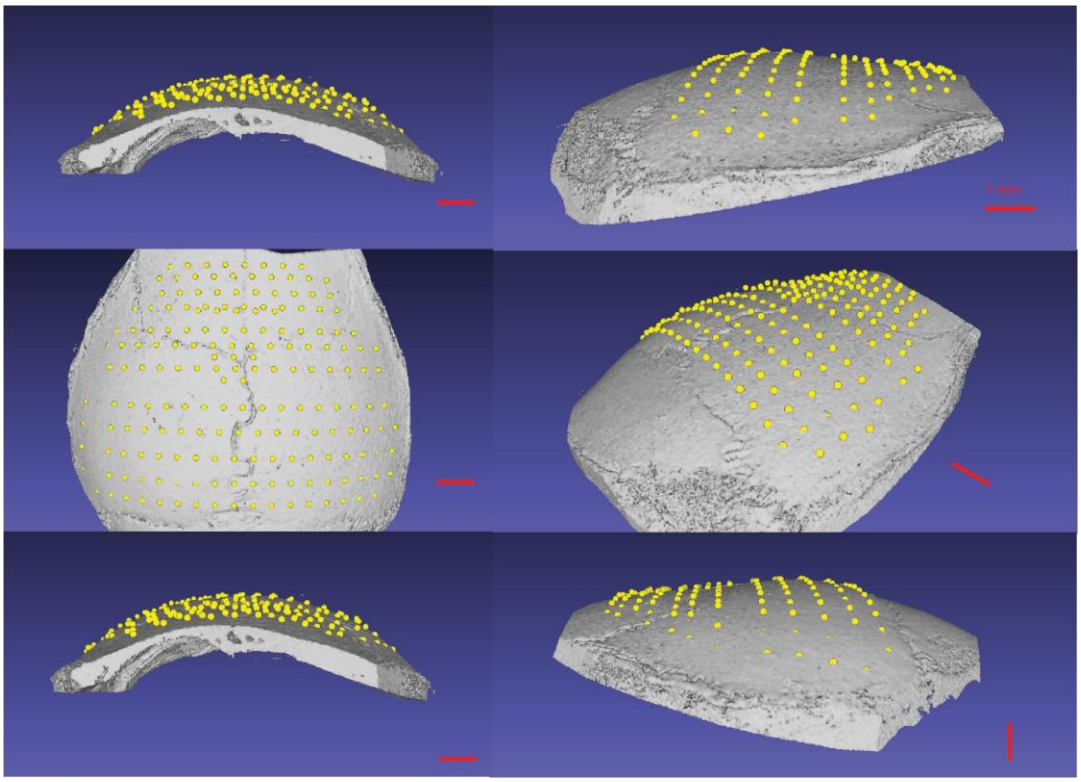

Figure 4.1: Average point cloud scan superimposed onto micro-CT. The average point cloud generated by scanning the dorsal cortex at 192 points five times superimposed on the micro-CT scan of the same skull qualitatively illustrates the accuracy of the contact sensor.

cloud consisting of 192-points spread across most of the dorsal skull surface. We then attached either a needle-tipped stylus or a 300-mm ruby-sphere tip stylus to the contact sensor and profiled the skull at these points. Five scans were performed on each mouse and we calculated the average point cloud generated from the surface profiler. This point

cloud was superimposed with a 3D reconstruction of the skull obtained via micro-CT scanning. One such superposition is illustrated in **Figure 4.1**. We found that the average point cloud of a male mouse scanned with the contact sensor fitted with the needle tip stylus mapped in 3D made a conforming fit when superimposed to the micro-CT scan of the skull of the same mouse (**Fig 4.1**). This was a qualitative indication that the contact

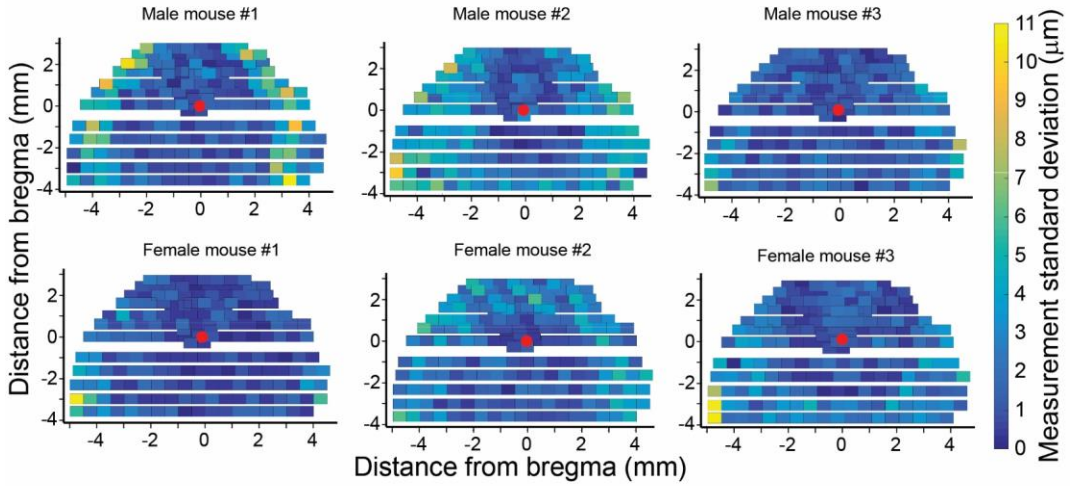

Figure 4.2: Standard deviation of point cloud scans vs displacement from bregma. Standard deviation of the measurements were plotted at the 192 scanned points on the dorsal surface from three male and three female mice.

sensor could accurately measure the topology of the dorsal skull surface. Following this, we set out to quantify the precision of the contact sensor. For each point on average point cloud of 192 points scanned on the mouse skull surface, we calculated the standard deviation. We plotted this data as a function of the displacement from bregma and this is illustrated in **Figure 4.2**. We also plotted the distribution of the measurement error in histogram form, and this is illustrated in **Figure 4.4**. We found that over 97% of the measurements had a measurement error less than 6 µm with the maximum error for all scans being 11 µm (**Table 4.1**).

Table 4.1: Precision of contact sensor

Maximum measurement error (μm)	1	2	3	4	5	6	7	8	9	10	11
Percent of scans	33.5%	61.4%	78.4%	88.0%	94.6%	97.4%	98.6%	99.1%	99.6%	99.7%	100.0%

Qualitatively, we observed that higher error was observed at lateral extremes on the skull surface, where the instantaneous slope of the surface could have possibly contributed to the error in measurements (**Fig. 4.2**). Given these observations, we assumed that the instantaneous slope and the measurement error for all mice were random variables, and measured the correlation between them. The contact sensor always approaches the skull in the vertical direction, so we examined if the instantaneous slope of the skull had an effect on the measurement, particularly with the ruby sphere stylus which may get actuated by forces acting at an angle to the normal axis. There was

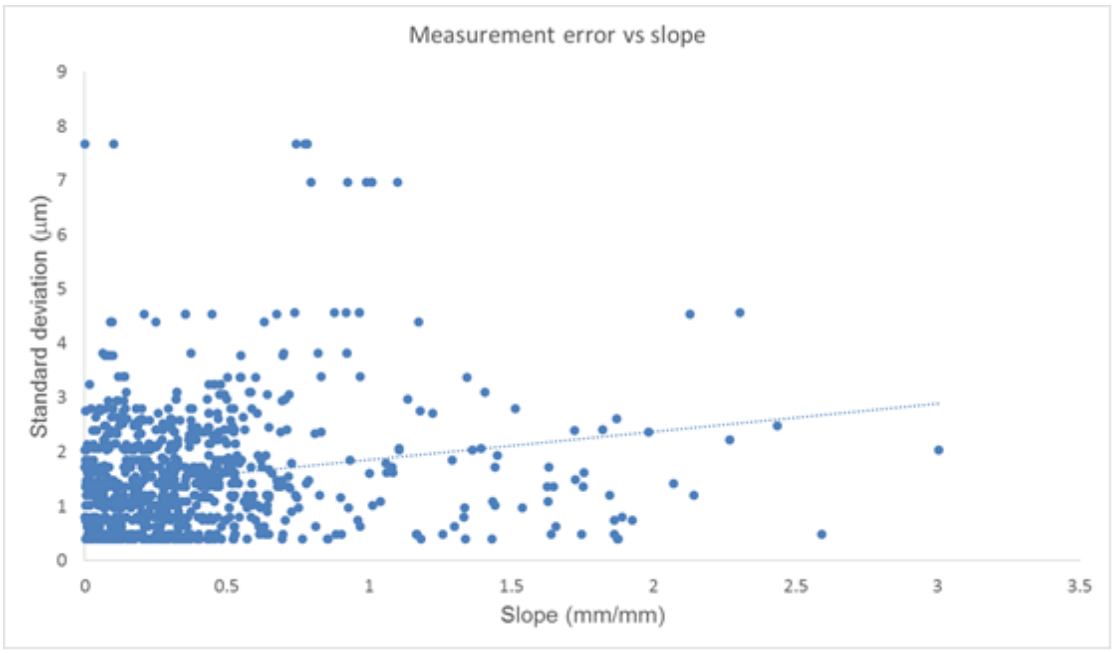

Figure 4.3: Standard deviation vs slope at scanned points. We intended to visualize the effect of the slope the skull surface on the precision of the contact sensor, but we found that the effect is very slight. A linear regression fails to explain the variance ($R^2 = 0.033$)

a slight correlation of measurement error of slope (r = 0.18). This was also observed when we visualized the measurement error vs slope in a scatter plot (**Fig 4.3**).

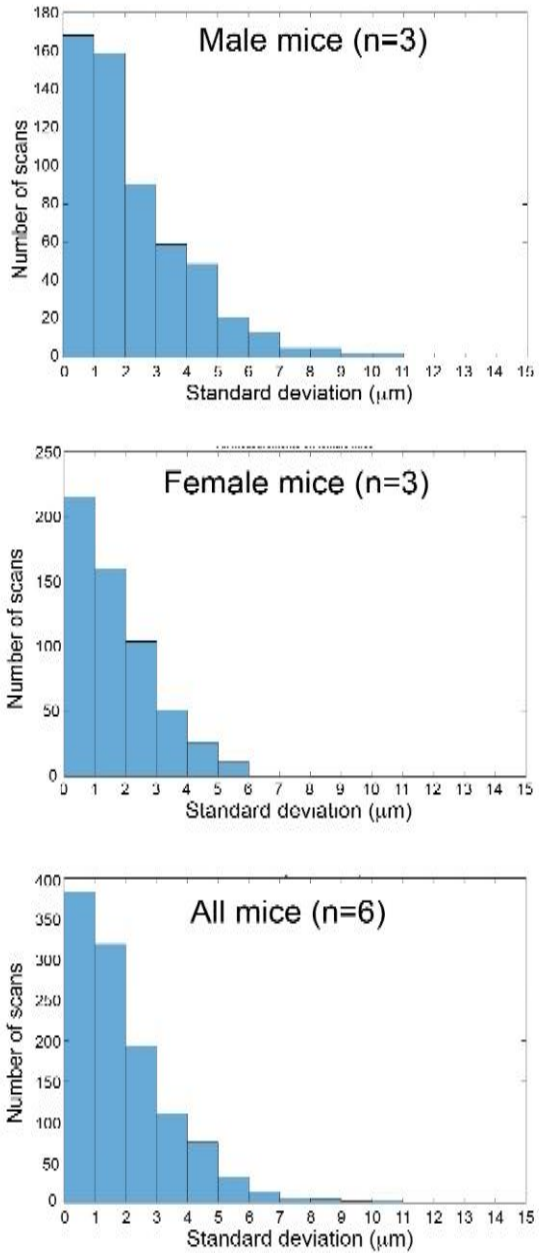

Figure 4.4: Histogram of measurement error.

We analyzed if the sex of the mouse affected the precision of surface profiling, and found that on average measurement error was 2.5 ± 11.9 μm for female mice, and 2.2 ± 1.8 μm for male mice. We also compared the measurement means on female and male

mice to test if the difference was statistically significant. We found that measurements on both sexes had a statistically insignificant difference in the mean error ($p = 0.62$, t-test).

We also compared the precision of the ruby sphere stylus tip vs the needle stylus tip for skull surface profiling, and found that the differences in the average measurement error were statistically insignificant when measured against each other ($p = 0.1288$, t-test).

Given that in our preliminary investigations, stopping drilling on an average 56 μm prior to reaching the lower surface of the skull was enough to fracture and excise the bone when performing a craniotomy, if we can use the measurements we obtain using the contact sensor to precisely guide the cutting tool within this value, CNC microsurgical procedures could be performed.

Chapter 5 Surface profile guided machining

Once we established that we had a robust and accurate means of profiling the surface of the skull, we wanted to examine how well we could use the information from surface profiling to guide the CNC machine to perform microsurgical procedures. Continuing our investigation of the effect of instantaneous slope on the accuracy of the measurement by the contact sensor, we asked whether this influences the ability of the Craniobot to accurately track the surface profile information to perform desired machining using a vertically-oriented tool. Further, we had to account for the diameter of the machine

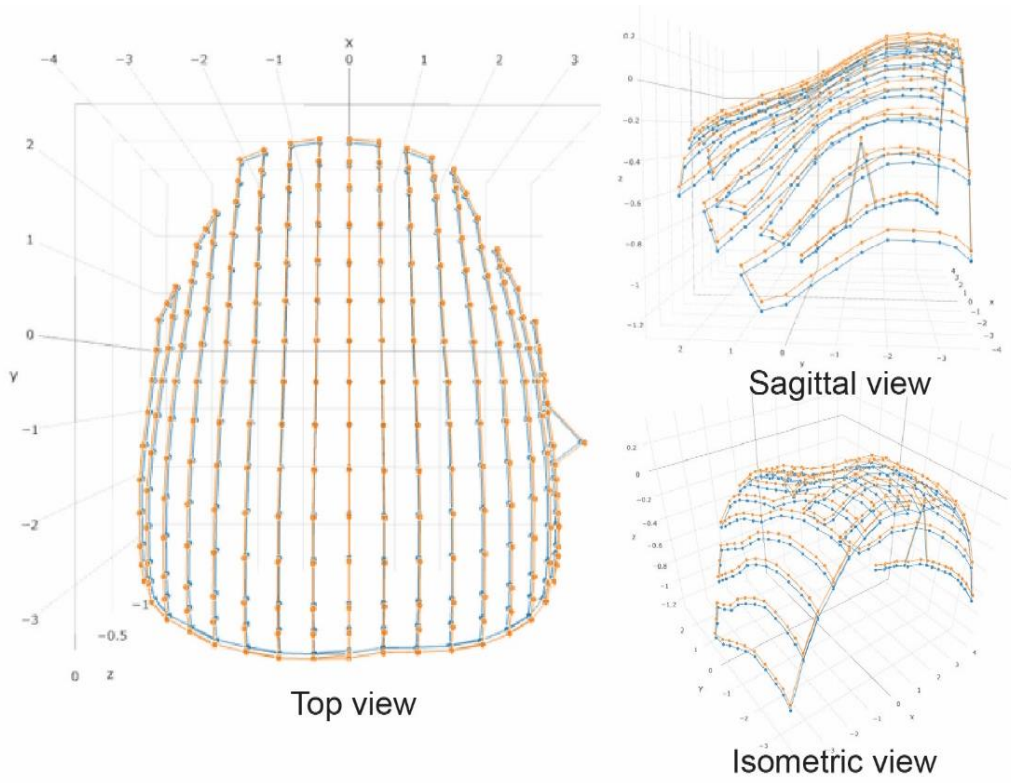

Figure 5.1: Test milling path. We made a test milling path for determining how well the surface profiling guided machining would perform across the dorsal skull surface. The orange points show the trajectory of the path generated from scanning at the surface, and the blue points show the path generated for milling guiding the cutting tool in the milling process.

tools and the stylus being used for surface profiling. We designed a stereotypical milling path that guided a CNC tool to mill 50 µm trenches along the anterior-posterior axis. The test milling path pilot points are illustrated in **Figure 5.1** along with the corresponding milling path generated by offsetting the automatic surface profiling. We used this information to test different cutting tools: a 200 µm square end mill, and a 300 µm ball end mill, resembling commonly used dental burrs.

5.1 Methods

Experiments were conducted by using the Craniobot to profile the surface in the stereotypical test path where the maximum spacing between pilot points was 0.5 mm, and the trenches were separated by 0.5 mm. We performed experiments where surface profiling was carried out using either the needle-tip or the ruby sphere tip stylus, and then used either the 200 µm square end mill or a 300 µm ball end mill, creating four unique conditions. We anticipated that we would observe differences in how the method of surface profiling affects the depth of trench milling at different locations on the skull surface. After milling, the mice were immediately perfused, and the skull surface was gently cleaned using cotton tips soaked in saline to remove blood and other bone debris from the trenches, after which the skulls were preserved in 4% PFA.

We used the Keyence VHX-5000E Digital microscope (Minnesota Nano Center, University of Minnesota) to reconstruct a 3D image of the skull surface after milling. A magnification of 1500X was used, yielding a resolution of 2.1 µm. We used the 3D image to calculate the depth of the trench, and the slope in the y direction and x direction with respect to z, dy/dx and dy/dz respectively. To find the depth of the trench with respect to the position measured by the contact sensor, a linear interpolation was used from one end

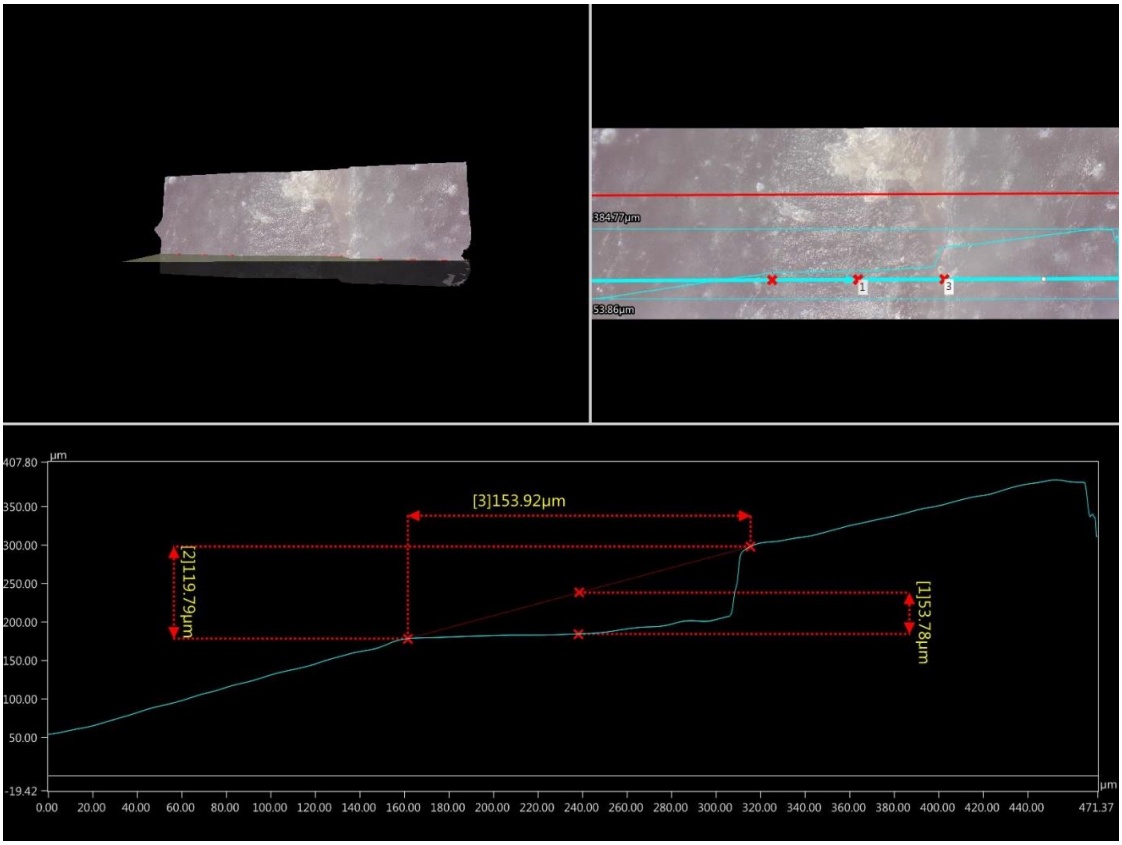

Figure 5.2: Measuring trench depth using the Keyence digital microscope software.

of the cut to the other. The slope dz/dx was calculated from the dimensions of this linear interpolation. The value of dz/dy was calculated using the same procedure in the y-direction. Measurements were performed every 500 µm, except when residuals such as bone fragments and blood were present. It often occurred that blood vessels in the skull were damaged, inundating the drilling trenches with blood and preventing accurate data measurements. **Figure 5.2** illustrates a sample measurement using the microscope and its accompanying software used for these measurements.

5.2 Performance of surface profile guided machining

To characterize the effects of the skull topology on capability of these four unique conditions to make 50 μm trenches, we sought to evaluate whether there was a trend in the depth of the cut due to the slope of the skull using linear regression analysis. For each condition, we obtained an average trench depth. For the combination of the needle tip stylus and the 300 μm ball end mill, we found the average trench depth to be 44.2 ± 5 μm, and we found the average trench depth to be 96.4 ± 19 μm for the combination of the needle tip stylus and 200 μm square end mill. For the two different cutting tools with the ruby-sphere stylus, we found the average trench depth to be 64.0 ± 5 μm with the 300 μm ball end mill and 57.3 ± 6 μm for the combination of the ruby sphere stylus and 200 μm square end mill (**Table 5.1, Figure 5.3**).

Table 5.1: Statistical analysis of probing tool and end mill combinations

Tool combination	Figure 5.3	p-value	Sample Size	Depth of Cut 95% Confidence Interval (μm)
Needle tip stylus and 300 μm ball-end mill	(a)	0.284	78	44.2 ± 5
	(b)	0.135	78	
Needle tip stylus and 200 μm square end mill	(c)	0.082	27	96.4 ± 19
	(d)	0.757	27	
Ruby sphere stylus and 300 μm ball end mill	(e)	0.008*	80	64.0 ± 5
	(f)	0.056	80	
Ruby sphere stylus and 200 μm square end mill	(g)	0.983	116	57.3 ± 6
	(h)	0.124	70	

Given that the measurements were taken at locations independent of the locations of the pilot points, we anticipated some variability due to the linearly interpolated tool path between the pilot points during milling. When compared to the target value of 50 μm, the needle tip stylus and the 300 μm ball end mill combination performed closest to target.

Further, we tested whether the slopes in the anterior-posterior and medial-lateral

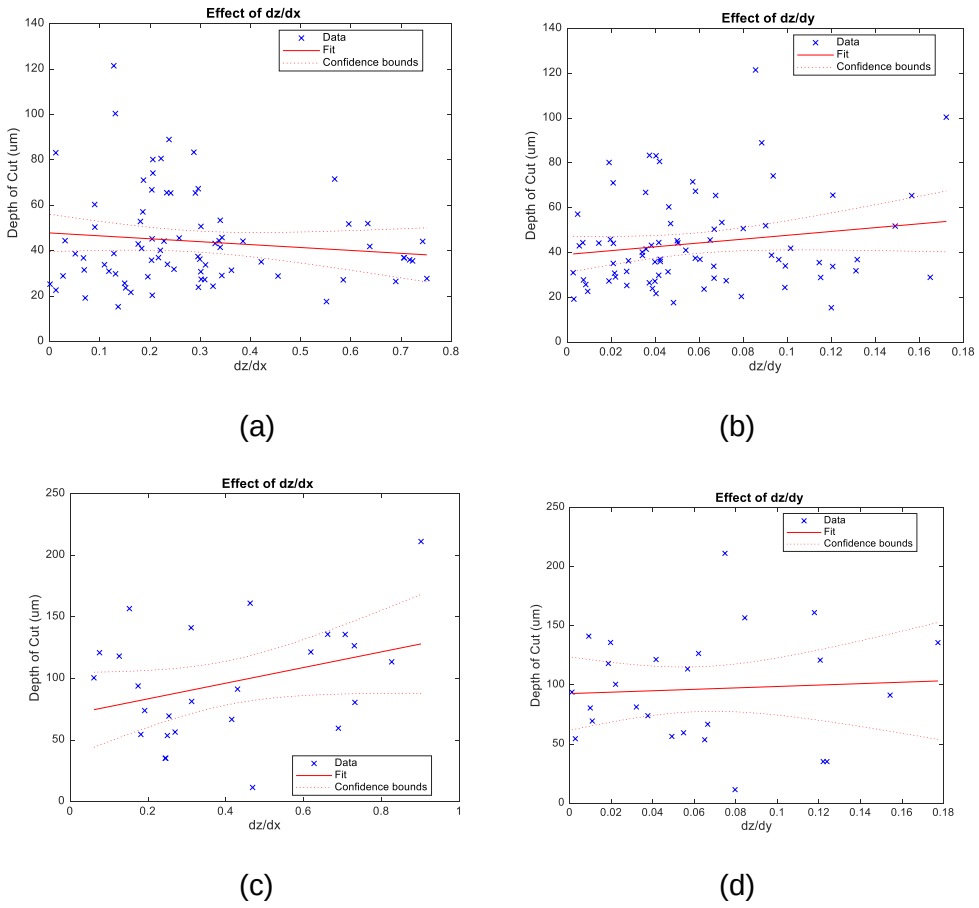

Figure 5.3.1: Linear regression performed for combinations of needle tip stylus and drill bits. The graphs show linear regression on the following tool combinations: needle tip stylus and 300 μm ball end (a) and (b), needle tip stylus and 200 μm square end (c) and (d).

directions affected the depth of trench drilling in each of the four conditions. The measured

trench depth as functions of the slope in the anterior-posterior and medial-lateral directions are illustrated in **Figure 5.3.1** and **Figure 5.3.2**. From the linear regression analysis, only

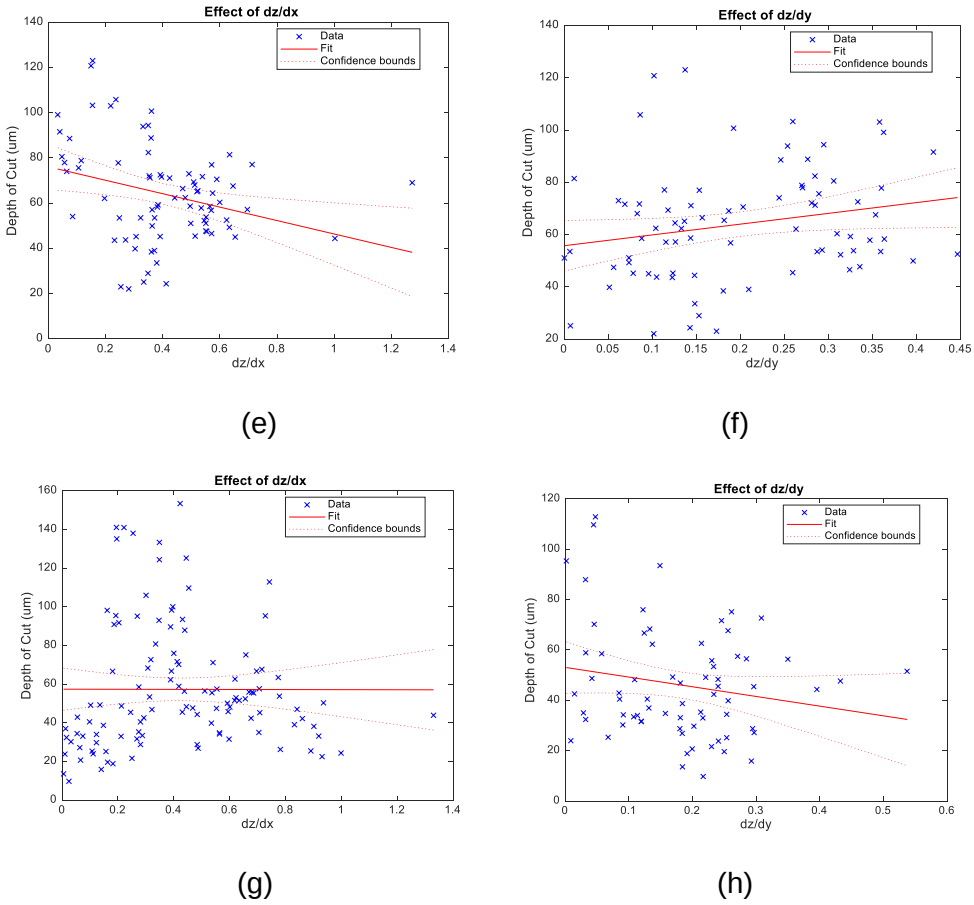

Figure 5.3.2: Linear regression performed for combinations of ruby sphere stylus and drill bits. The graphs show linear regression on the following tool combinations: ruby sphere stylus and 300 μm ball end (e) and (f), ruby sphere stylus and 200 μm square end (g) and (h).

the combination of ruby sphere probe and the 300 μm ball end mill displayed a statistically significant relationship between the depth of cut and the slope in the medial-lateral direction ($p = 0.008$). In the other cases, the analysis failed to reject the assumption that the slope of the skull has no effect on the depth of cut. Based upon these results, we can conclude that the Craniobot is not only capable of precisely mapping the skull surface, but

it is also able to perform precise machining operations across a wide swathe of the dorsal skull on stereotaxically-fixed mice. In the next chapter, we describe and illustrate some of these capabilities.

Chapter 6 Demonstration of microsurgical procedures

Some of the more challenging procedures are skull excisions for cranial windows, skull thinning, and drilling pilot holes. In this chapter, we illustrate each of these performed by the Craniobot.

6.1 Methods

All demonstration procedures performed with the Craniobot used a 300 μm ruby-sphere stylus tip on the contact sensor. Mice were anesthetized according to the methods described in **Section 4.1.1**. To perform skull excisions, we used a 200 μm square end mill to iteratively mill at increasing depths until the skull fragment was ready to be excised. The method described in **Section 4.1.3** was used to implant 2 male wild type C57BL/6J mice, 10 and 12 weeks old with 4 mm diameter circular coverslips.

One canonical procedure used to gain optical access to the brain in behaving animals without disturbing the brain are skull thinning experiments as described by Drew et al. and Shih et al. (Drew et al., 2010; Shih et al., 2012)). This procedure is performed by thinning and polishing the skull using a drill and various other tools. To perform such skull thinning procedures with the Craniobot, we increased the density of points. This allowed a 300 μm ball end mill to mill paths that were overlapping to uniformly thin the skull. The maximum distance between points the contact sensor scanned the skull surface was decreased to 0.15 mm for increased precision. We used a milling depth of 110 μm as our maximum depth to thin the skull.

6.2 Results of automated microsurgical procedures

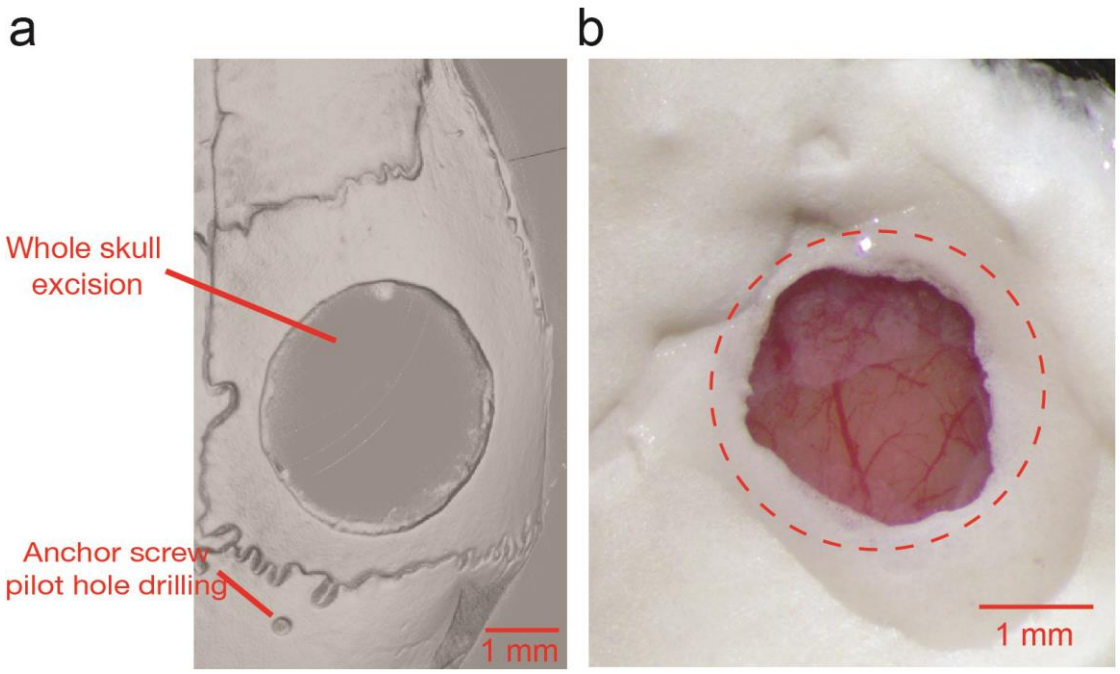

Figure 6.1: Demonstration of skull excisions for circular coverslip implantations. Shown here are two mice which the same microsurgical procedure was performed with the Craniobot. (a) shows a micro-CT scan of an adult male C57BL6/J mouse for which an automated circular craniotomy was performed, and (b) shows another mouse implanted with a cicrcular coverslip after the same microsurgical procedure was performed at 2 weeks of implantation. The Craniobots capability to drill anchor screw pilot holes is also demonstrated in the micro-CT scan in (a)

We demonstrate the capability of the Craniobot to perform automated skull excisions and drilling of anchor holes for skull screws, in **Figure 6.1a**. Another mouse implanted with the same microsurgical procedure with a circular coverslip is shown two weeks after implantation in **Figure 6.1b**.

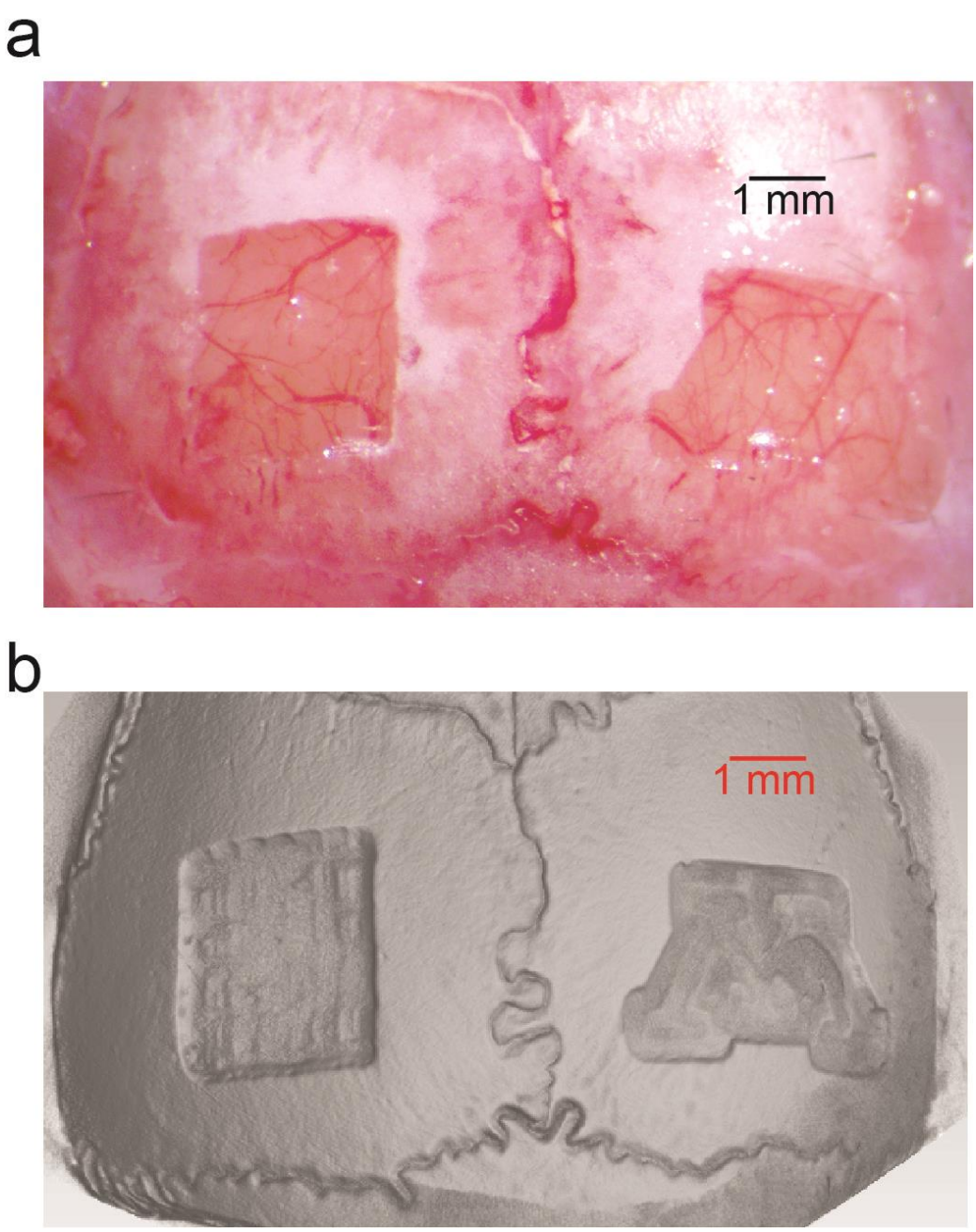

Figure 6.2: Automated skull thinning for optical access. The skull was thinned by 110 mm in a 2x2 mm square, and 100 mm in the shape of a University of Minnesota 'M' on an adult male wild type C57BL/6J mouse 10 weeks old. After the experiment, the mouse was perfused and the skull was collected for micro-CT scanning. (a) Shows a photograph taken of the mouse shortly after the skull thinning procedure, emphasizing increase in optical access. Saline was used for refractive index matching after the skull thinning procedure. A micro-CT scan of the same mouse rendered in 3D is shown in (b), confirming skull thinning without damage to the underlying tissue.

6.2a shows a photograph of a mouse's skull thinned to 110 μm in the shape of a 2x2 mm square with dimensions of 2x2 mm and thinned to 100 μm in the shape of a University of Minnesota logo to demonstrate the precision of the Craniobot.

Chapter 7 Conclusion

We have introduced a novel automated surface profiling methodology applied to a CNC mill adapted to perform microsurgical procedures. We demonstrated that the automated skull surface profiling method is precise on skull tissue, and it is sufficient to perform microsurgical procedures across the skull surface of the skull above the mice dorsal cortex. These procedures include craniotomies, and skull thinning for optical access, enabling the Craniobot to be incorporated for many *in vivo* neuroscience applications. The Craniobot thus enables the exploration of complex neuroscience research by a much more diverse set of neuroscience labs by decreasing entry barriers due to time taken training and cost of performing complex surgical procedures. Additionally, the Craniobot enables deeper investigation utilizing already existing complex surgeries.

Furthermore, the Craniobot's microsurgical procedure platform is generalizable owing to its mostly open source implementation and the use of highly developed precision machining tools. These enable the high flexibility and expandability of the Craniobot's capabilities, possibly exploring more complex procedures in mice, or larger animal models.

Currently, microsurgical procedures such as craniotomies and skull thinning are performed iteratively, increasing the time taken and lacking feedback information from the operated skull tissue. Closing the loop by providing information about the milled tissue through the drill or via another added capability would increase the viability of the Craniobot even further for simple and complex surgical procedures. This could possibly be implementing via the impedance sensing method explored by Pak et al (Pak et al.,

2015), or another highly developed modality. Presently, the ultra-precise single to ten-micrometer precision of the skull surface profiling is sufficient to perform microsurgical procedures. While this precision is well within the limits of microsurgical procedures performed, if a microsurgical procedure required anything even more complex/precise, a tilt axis for improved probing precision at the lateral extremes or other irregular surfaces could also be included to the profiling procedure.

The surgical methodologies discussed thus far have been developed predominantly in mice. With the advent of new genetic tools such as CRISPR, it will be possible soon to rapidly generate genetically modified model organisms in species such as rats and nonhuman primates that provide capabilities beyond mice. Generalized strategies to extend complex surgical procedures optimized in mice to other species will be very useful. Automation tools such as those implemented in the Craniobot can enhance our abilities to perform such operations, reducing experimental variability and enhancing throughput. This could bolster emerging industrial scale neuroscience initiatives such as the Blue Brain Project (Markram, 2006), connectomics (Bohland et al., 2009), and Allen Brain Maps (Oh et al., 2014). By automating the most difficult aspects of *in vivo* neuroscience procedures, the Craniobot could streamline these neuroscience pipelines and allow systematic studies to generate vast datasets that are more consistent across experiments with ease.

Bibliography

Agiimaa Kruchkin. (2016). Innovation in Creation: Demand Rises While Prices Drop for 3D Printing Machines : Media Center. Retrieved April 18, 2017, from https://www.ibisworld.com/media/2016/02/16/innovation-in-creation-demand-rises-while-prices-drop-for-3d-printing-machines/

Blanche, T. J. (2005). Polytrodes: High-Density Silicon Electrode Arrays for Large-Scale Multiunit Recording. *Journal of Neurophysiology*. https://doi.org/10.1152/jn.01023.2004

Bohland, J. W., Wu, C., Barbas, H., Bokil, H., Bota, M., Breiter, H. C., … Mitra, P. P. (2009). A Proposal for a Coordinated Effort for the Determination of Brainwide Neuroanatomical Connectivity in Model Organisms at a Mesoscopic Scale. *PLoS Computational Biology*, *5*(3), e1000334. https://doi.org/10.1371/journal.pcbi.1000334

Boyden, E. S., Zhang, F., Bamberg, E., Nagel, G., & Deisseroth, K. (2005). Millisecond-timescale, genetically targeted optical control of neural activity. *Nature Neuroscience*, *8*, 1263. Retrieved from http://dx.doi.org/10.1038/nn1525

Drew, P. J., Shih, A. Y., Driscoll, J. D., Knutsen, P. M., Blinder, P., Davalos, D., … Kleinfeld, D. (2010). Chronic imaging and manipulation of cells and vessels through a polished and reinforced thinned-skull. *Nature Methods*, *7*(12), 981–984. https://doi.org/10.1038/nmeth.1530

Holtmaat, A., Bonhoeffer, T., Chow, D. K., Chuckowree, J., De Paola, V., Hofer, S. B., … Wilbrecht, L. (2009). Long-term, high-resolution imaging in the mouse neocortex

through a chronic cranial window. *Nature Protocols*, *4*, 1128. Retrieved from http://dx.doi.org/10.1038/nprot.2009.89

HUBEL, D. H. (1957). Tungsten Microelectrode for Recording from Single Units. *Science*, *125*(3247), 549–550. https://doi.org/10.1126/science.125.3247.549

Jun, J. J., Steinmetz, N. A., Siegle, J. H., Denman, D. J., Bauza, M., Barbarits, B., … Harris, T. D. (2017). Fully integrated silicon probes for high-density recording of neural activity. *Nature*, *551*, 232. Retrieved from http://dx.doi.org/10.1038/nature24636

Khodagholy, D., Gelinas, J. N., Zhao, Z., Yeh, M., Long, M., Greenlee, J. D., … Buzsáki, G. (2016). Organic electronics for high-resolution electrocorticography of the human brain. *Science Advances*, *2*(11), e1601027. https://doi.org/10.1126/sciadv.1601027

Kim, T. H., Zhang, Y., Lecoq, J., Jung, J. C., Li, J., Zeng, H., … Schnitzer, M. J. (2016). Long-Term Optical Access to an Estimated One Million Neurons in the Live Mouse Cortex. *Cell Reports*, *17*(12), 3385–3394. https://doi.org/10.1016/j.celrep.2016.12.004

Kodandaramaiah, S. B., Franzesi, G. T., Chow, B. Y., Boyden, E. S., & Forest, C. R. (2012). Automated whole-cell patch-clamp electrophysiology of neurons in vivo. *Nature Methods*, *9*(6), 585–587. https://doi.org/10.1038/nmeth.1993

Kodandaramaiah, S. B., Holst, G. L., Wickersham, I. R., Singer, A. C., Franzesi, G. T., McKinnon, M. L., … Boyden, E. S. (2016). Assembly and operation of the autopatcher for automated intracellular neural recording in vivo. *Nature Protocols*, *11*(4), 634–654. https://doi.org/10.1038/nprot.2016.007

Liu, J., Fu, T. M., Cheng, Z., Hong, G., Zhou, T., Jin, L., … Lieber, C. M. (2015). Syringe-

injectable electronics. *Nature Nanotechnology*, *10*(7), 629–635. https://doi.org/10.1038/nnano.2015.115

Markram, H. (2006). The Blue Brain Project. *Nature Reviews Neuroscience*, *7*, 153. Retrieved from http://dx.doi.org/10.1038/nrn1848

Oh, S. W., Harris, J. A., Ng, L., Winslow, B., Cain, N., Mihalas, S., … Zeng, H. (2014). A mesoscale connectome of the mouse brain. *Nature*, *508*, 207. Retrieved from http://dx.doi.org/10.1038/nature13186

Pak, N., Siegle, J. H., Kinney, J. P., Denman, D. J., Blanche, T. J., & Boyden, E. S. (2015). Closed-loop, ultraprecise, automated craniotomies. *Journal of Neurophysiology*, *113*(10), 3943–3953. https://doi.org/10.1152/jn.01055.2014

Pisanello, F., Mandelbaum, G., Pisanello, M., Oldenburg, I. A., Sileo, L., Markowitz, J. E., … Sabatini, B. L. (2017). Dynamic illumination of spatially restricted or large brain volumes via a single tapered optical fiber. *Nature Neuroscience*, *20*(8), 1180–1188. https://doi.org/10.1038/nn.4591

Scholvin, J., Kinney, J. P., Bernstein, J. G., Moore-Kochlacs, C., Kopell, N., Fonstad, C. G., & Boyden, E. S. (2016). Close-Packed Silicon Microelectrodes for Scalable Spatially Oversampled Neural Recording. *Biomedical Engineering, IEEE Transactions on*, *63*(1), 120–130. https://doi.org/10.1109/TBME.2015.2406113

Shih, A. Y., Mateo, C., Drew, P. J., Tsai, P. S., & Kleinfeld, D. (2012). A Polished and Reinforced Thinned-skull Window for Long-term Imaging of the Mouse Brain. *Journal of Visualized Experiments : JoVE*, (61), 3742. https://doi.org/10.3791/3742

Silasi, G., Xiao, D., Vanni, M. P., Chen, A. C. N., & Murphy, T. H. (2016). Intact skull chronic windows for mesoscopic wide-field imaging in awake mice. *Journal of*

Neuroscience Methods, *267*, 141–149. https://doi.org/10.1016/j.jneumeth.2016.04.012

Suk, H.-J., Welie, I. Van, Kodandaramaiah, S. B., Allen, B., Forest, C. R., Boyden, E. S., … Forest, C. R. (2017). Closed-Loop Real-Time Imaging Enables Fully Automated Cell-Targeted Patch-Clamp Neural Recording In Vivo NeuroResource Closed-Loop Real-Time Imaging Enables Fully Automated Cell-Targeted Patch-Clamp Neural Recording In Vivo. *Neuron*, *95*(5), 1037–1046.e11. https://doi.org/10.1016/j.neuron.2017.08.011

Viventi, J., Kim, D.-H., Vigeland, L., Frechette, E. S., Blanco, J. A., Kim, Y.-S., … Litt, B. (2011). Flexible, foldable, actively multiplexed, high-density electrode array for mapping brain activity in vivo. *Nature Neuroscience*, *14*, 1599. Retrieved from http://dx.doi.org/10.1038/nn.2973

Wang, Y., Liu, Y., Wang, S., & Wang, Z. (2016). In vivo whole-cell recording with high success rate in anaesthetized and awake mammalian brains. *Molecular Brain*, *9*(1), 86. https://doi.org/10.1186/s13041-016-0266-7

Yazicioglu, F., Lopez, C. M., Mitra, S., Raducanu, B., Musa, S., & Kloosterman, F. (2014). Ultra-high-density in-vivo neural probes. *Conference Proceedings : ... Annual International Conference of the IEEE Engineering in Medicine and Biology Society. IEEE Engineering in Medicine and Biology Society. Annual Conference*, *2014*.

Zong, W., Wu, R., Li, M., Hu, Y., Li, Y., Li, J., … Cheng, H. (2017). Fast high-resolution miniature two-photon microscopy for brain imaging in freely behaving mice. *Nature Methods*, *14*, 713. Retrieved from http://dx.doi.org/10.1038/nmeth.4305